Bull. Mater. Sci. (2024) 47:123
https://doi.org/10.1007/s12034-024-03195-3

Analysing the impact of Dy dopants on Zn-based hydroxyapatites: modelling and characterization perspectives

OZNUR BÜYÜK[1], NIYAZI BULUT[1,*], M MURSIT TEMUZ[2], CAHIT OREK[1], TANKUT ATES[3], OMER KAYGILI[1], İMREN ÖZCAN[4] and ALI KURUÇAY[4]

[1]Department of Physics, Faculty of Science, Firat University, 23119 Elazig, Turkey
[2]Department of Chemistry, Faculty of Science, Firat University, 23119 Elazig, Turkey
[3]Department of Engineering Basic Sciences, Faculty of Engineering and Natural Sciences, Malatya Turgut Özal University, 44270 Battalgazi, Malatya, Turkey
[4]Department of Chemistry, Faculty of Arts and Science, Inonu University, 44280 Malatya, Turkey
*Author for correspondence (bulut_niyazi@yahoo.com)

MS received 15 September 2023; accepted 8 January 2024

Abstract. This study is aimed to investigate the effects of introducing dysprosium (Dy) into Zn-based hydroxyapatite (HAp) at various concentrations (0.45, 0.90, 1.35 and 1.80%). The structural and optical properties of pure and doped HAp were thoroughly examined through theoretical and empirical analyses, including X-ray diffraction, Raman spectroscopy and Fourier transform infrared (FTIR) studies. The results confirmed the successful incorporation of Dy into the HAp lattice without significantly affecting its thermal stability or stoichiometry. The introduction of Dy into Zn-based HAp led to notable alterations in several material parameters. The lattice parameters, crystallinity, lattice stress, strain and anisotropic energy density varied with different Dy concentrations. In comparison with undoped HAp, all Dy-doped Zn-based HAps exhibited reduced crystallite size values, indicating a change in the microstructure. Furthermore, the material density increased from 3.159 to 3.228 g cm^{-3} with Dy doping. The band gap (BG), an important parameter for optical applications, is consistently decreased from 4.6 to 3.9 eV as the Dy concentration increased. This decrease in BG suggests the potential for improved photocatalytic or optoelectronic properties in Dy-doped Zn-based HAp. Additionally, the linear absorption coefficient (LAC) increased, indicating enhanced light absorption. Overall, this study provides a comprehensive understanding of structural and optical modifications induced by Dy doping in Zn-based HAp. These findings contribute to the potential application of Dy-doped Zn-based HAp in various fields, including biomedicine, photocatalysis and optoelectronics.

Keywords. Hydroxyapatite; DOS; LAC; band structure.

1. Introduction

An essential part of the bioceramic group of biomaterials, hydroxyapatite ($Ca_{10}(PO_4)_6(OH)_2$) has a chemical and biological structure that is comparable to the inorganic components of bones and teeth and exhibits similar qualities. It is therefore, one of the most promising calcium phosphate ceramic materials for the creation of bone implants and prostheses, coatings on dental implants, due to its ability to chemically attach to bone [1–4].

Apatite, also known as hydroxyapatite or HAp, belongs to the apatite family ($A_{10}(BO_4)_6X_2$) [5] and has a mole ratio of Ca/P of 1.67. There are two recognized phases of the HAp crystal: hexagonal and monoclinic. The typical hexagonal crystal structure of biological or synthetic HAp includes two primary crystal planes of '*a*' with a positive charge and '*c*' having a negative charge [6–9]. The 44 atoms that make up the unit cell are divided into two non-equivalent crystallographic areas, two types of calcium atoms (Ca-I and Ca-II) and six tetrahedral phosphate groups (PO_4).

HAp has excellent osteoconductivity, osteoinductivity, biofunctionality, high chemical and thermal stabilities, porous structure, pyroelectric and piezoelectric properties that help it to respond to mechanical stress as well as good biocompatibility, bioactivity, low cost, non-toxicity and chemical similarity with the inorganic content of calcified tissues. It has a variety of qualities, including the capacity for molecules to be absorbed by it and subsequently, cure bone flaws instantly [1,3,9–12]. Owing to these superior qualities, HAp is used in numerous fields, including electro- and photo-catalysis, sensors, bio-magnetic particles, bone cement, protein delivery, drug delivery and tissue engineering [9]. It is also one of the most preferred scaffold materials in the regeneration of diseased or damaged bone and teeth [9–11,13–15].

Published online: 07 June 2024

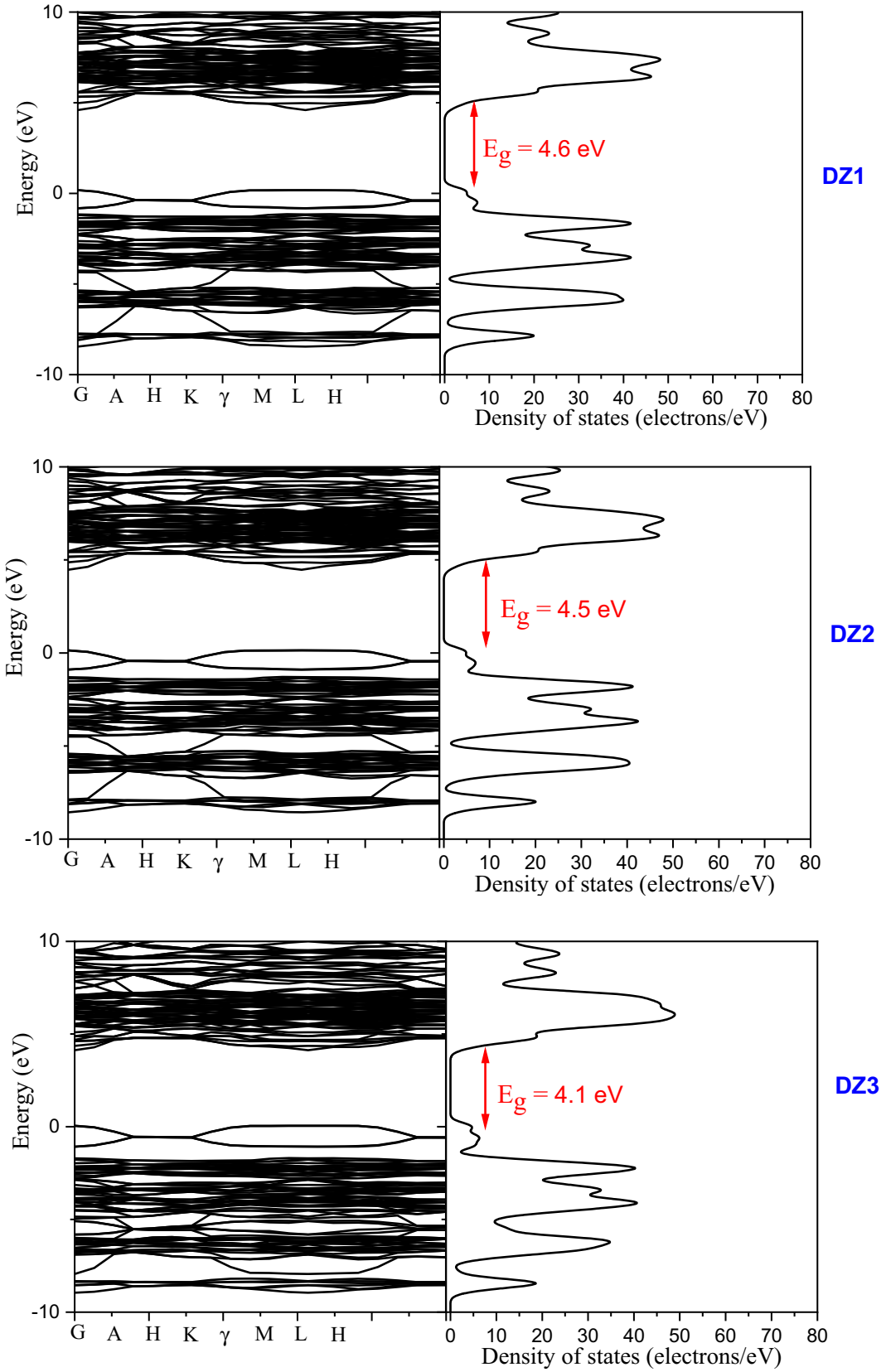

Figure 1. Band structure and density of states of Dy-doped Zn-based HAp structures.

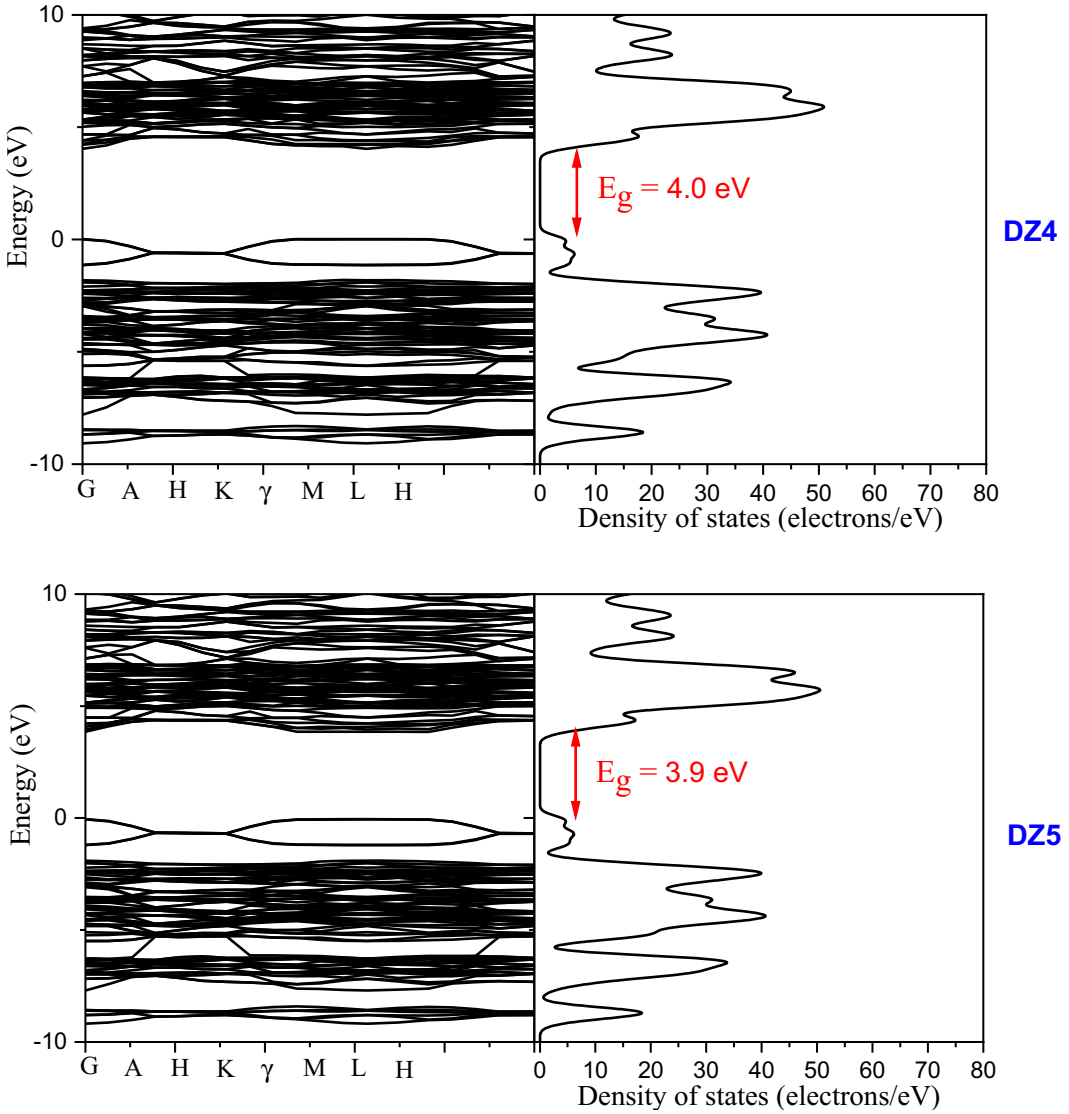

Figure 1. continued

Numerous processes are used to produce hydroxyapatite, both naturally and artificially. Plants, algae, limestone, bones of mammals like cattle, camels and horses, waste materials like fish bones and scales, egg shells, oysters and seashells and biological resources are some examples of natural resources from which we might extract hydroxyapatite [2]. Sol–gel [16], wet chemical precipitation [17], hydrothermal [18], spray freezing [19], sonochemical [20], hydrolysis [21], emulsion [22], microwave [23], mechanochemical [24] and solid-state [25] are synthetic methods for producing hydroxyapatite powder.

Numerous investigations have been conducted recently regarding the enhancement of numerous hydroxyapatite characteristics, particularly, through doping [2]. HAp structure, Bi [26], Mn [27], B [28], Ce [29], Sr [30], Ti [31], Al [32], Cu [33], Mg [34] and Ag are all mentioned in the literature. Numerous features of elements including Ni [35], Zn [36], Dy [37], Er [38], Nd [39] and Yb [40] are observed to be enhanced by doping. Zn-doped HAp in *Escherichia* sp. and *Staphylococcus aureus* had high bioactive and antibacterial activities, according to Ofudje *et al* [41]. Buyuksungur *et al* [42] concluded that zinc can be added to the HAp structure to improve its mechanical and antibacterial qualities, while maintaining its biological and corrosion-resistant features. It was reported that the amount of Zn is below 1%, generally, its adverse effects were not observed [43]. In contrast, its higher amounts caused a decrease in the crystallinity and weak interfacial interactions. According to studies, the properties of rare earth element Dy, which is added to the HAp structure, are improved. Dy is one of the rare-earth elements. According to Tesch *et al* [44], Dy-doped HAp displayed paramagnetic behaviour and non-toxic characteristics as a result of the doping of Dy^{3+} with a strong magnetic moment. Dy^{3+}-doped synthetic hydroxyapatite produced by co-precipitation technique, as determined by Rout and Agrawal [7], is a

possible component for hot light-emitting diodes. Using the chemical sonication approach, Bulcar *et al* [37] produced Dy-doped hydroxyapatite materials and examined the impact of ion doping and changes in doping concentration on the structure and thermoluminescence of the material. By co-precipitation, Lafarga *et al* [45] created dysprosium-doped hydroxyapatites. In the literature, many papers are related to Zn-doped HAps, whereas only a few studies about Dy-doped HAps exist. To our knowledge, no study was found on the experimental and theoretical characterization of Dy/Zn co-doped HAps. Additionally, the investigation of biocompatibilities of Dy-doped HAps is still incomplete.

The goal of the current study is to provide additional in-depth details regarding the impacts of Dy content on the structural, morphological, thermal and *in vitro* cell survival aspects of Zn-based HAp samples. Additionally, this study is the first to include theoretical computation results on the band gaps (BG), linear absorption coefficient (LAC) and density of states (DOS) of the undoped and Dy-doped Zn-HAp structures.

2. Experimental

Zn-based (0.45 at%) HAp and its Dy-doped (0.45, 0.90, 1.35 and 1.80 at.%) derivatives, with the formulations of $Ca_{9.955}Zn_{0.045}(PO_4)_6(OH)_2$, $Ca_{9.910}Zn_{0.045}Dy_{0.045}(PO_4)_6(OH)_2$, $Ca_{9.865}Zn_{0.045}Dy_{0.090}(PO_4)_6(OH)_2$, $Ca_{9.820}Zn_{0.045}Dy_{0.135}(PO_4)_6(OH)_2$ and $Ca_{9.775}Zn_{0.045}Dy_{0.180}(PO_4)_6(OH)_2$ were synthesized as: a 0.5 M solution of calcium nitrate tetrahydrate (Carlo-Erba) was mixed with ammonia (Sigma-Aldrich) and 0.3 M diammonium hydrogen phosphate (Merck), raising the pH to 10.5 in the process of zinc acetate dihydrate (Sigma-Aldrich) and dysprosium (III) nitrate hydrate (Sigma-Aldrich). The mixture was blended for 4.5 h at 65°C, then, it was dried for 37 h in a 120°C oven. This dry sample was calcined for 2 h at 900°C in an electric furnace. The Dy-containing HAp powders were obtained, and these samples were named DZ1, DZ2, DZ3, DZ4 and DZ5 according to the increasing amount of Dy-content from 0.45 to 1.80 at.%.

X-ray diffraction (XRD) data were collected using a Rigaku Rad B-DMAX II instrument, renowned for its accuracy in analysing crystal structures. Raman spectroscopy and Fourier transform infrared (FTIR) spectra were obtained using a PerkinElmer Spectrum One spectrophotometer and a UniDRON Raman microscope, respectively. The FTIR analysis involved the application of KBr technique, which utilizes potassium bromide as a sample matrix. Differential thermal analysis (DTA) was conducted using a Shimadzu DTA 50 device to investigate thermal behaviour and phase transitions. Morphological investigations were performed utilizing the FEI Quanta 450 FEG scanning electron microscope (SEM), enabling high-resolution imaging of surface features and structures.

L-929 mouse fibroblast cells were selected as the model system to assess the biocompatibility of the samples. These cells are commonly employed in cytotoxicity studies due to their sensitivity to various external factors and their ability to offer valuable insights into the interaction between materials and living cells. Our previous study [29] provides a comprehensive description of the experimental procedures involved, which encompassed sample preparation, seeding of L-929 mouse fibroblast cells onto the samples and subsequent assessment of cell viability through diverse assays. These assays encompassed measurements of cell proliferation, cell morphology, metabolic activity and cell viability markers, among others. By conducting these *in vitro* cell viability tests, our objective is to enhance our understanding of the biocompatibility and potential cytotoxic effects associated with the as-produced samples. The findings obtained from these experiments will significantly contribute to our overall evaluation of the samples' suitability for biomedical applications and furnish crucial insights into their interactions with living cells.

3. Results and discussion

3.1 *Theoretical results*

The band structure (BS) is a useful tool for visualizing the BG, potential electronic transitions and the wave vector dependence of the energy levels. Computing a BS or DOS is straightforward [46–48]. The states can be found at k-points on the BS or DOS after setting the ground state density, which we obtained through adequate k-point sampling. This is illustrated below using a symbolic geometry.

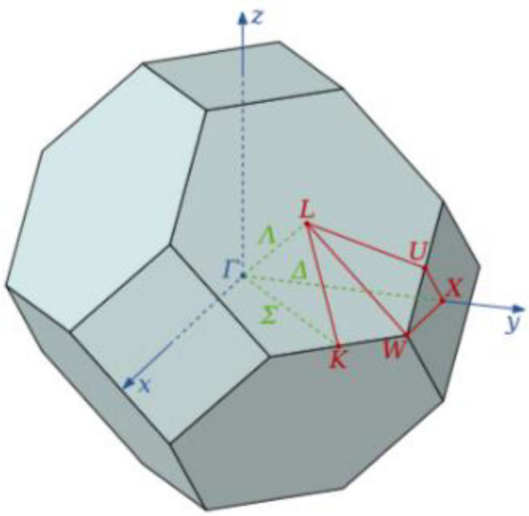

The reciprocal lattice vectors typically do not arrange themselves into a straightforward cubic lattice, and as a result, the Brillouin zone can assume various forms. It is

common practice to plot the energy solely along specific high-symmetry directions, considering that the wave vector, k, is a three-dimensional vector. The energies along these directions represent the maximum or lowest energy values for the bands across the entire Brillouin zone.

While the ground state calculation may require a larger number of k-points, it can actually be considerably faster since the density remains fixed for the computation of the BS or DOS itself. The carrier concentration can be written as:

$$n = \int_{E_C}^{\infty} g(E) f_F(e) dE. \quad (1)$$

In this equation, g represents the number of states per volume in a small energy range and can be defined as:

$$g(E) = 4\pi \left(\frac{2m_n^*}{h^2}\right)^{3/2} E^{1/2} \quad (2)$$

and f is Fermi energy as:

$$f_F(E) = \frac{1}{e^{(E-E_F)/kT} + 1}. \quad (3)$$

Theoretical calculations in this study were carried out using the CASTEP [49] software package, which is widely utilized for performing electronic structure calculations based on density functional theory (DFT). The DFT technique was employed to compute the BSs, which provide valuable information about the energy levels and electronic properties of the system under investigation. By employing DFT, the electronic structure and properties of the material can be accurately determined, facilitating a comprehensive understanding of its behaviour and characteristics.

The BSs of a material were investigated and depicted in figure 1, with the positions of the bands corresponding to specific intervals between the G and H points in the Brillouin zone. The obtained energy values are shown in the figure. Within the low- and high-energy ranges, a continuous spectrum is observed, indicating the presence of a wide range of energy levels. Notably, both the valence and conduction BSs appear to have a nearly flat shape in the same figure. In the case of a pure Zn-based hydroxyapatite (HAp) material, the highest energy point in the valence band is located at a variable wave vector denoted as $k = \gamma - H$. Conversely, the lowest energy point in the conduction band is situated at the wave vector, $k = \gamma - H$. The BG values corresponding to specific energy levels were determined for different regions, namely. DZ1, DZ2, DZ3, DZ4 and DZ5. The BG values for these regions are as follows: DZ1 (4.6 eV), DZ2 (4.5 eV), DZ3 (4.1 eV), DZ4 (4.0 eV) and DZ5 (3.9 eV). These values represent the energy gap between the valence and

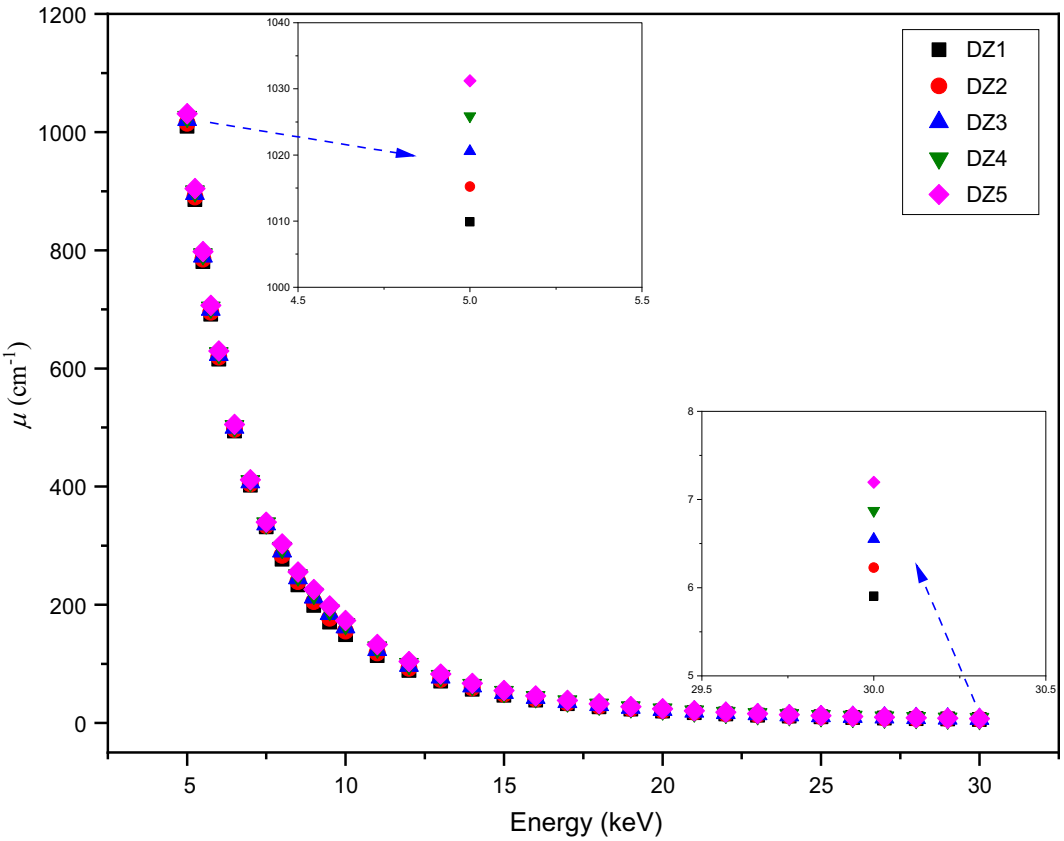

Figure 2. LAC *vs.* photon energy graphs of the un-doped and Dy-doped Zn-based HAp structures.

Table 1. As-estimated values from the modelling and XRD analysis.

	DZ1	DZ2	DZ3	DZ4	DZ5
Theoretical					
a (nm)	0.935	0.936	0.924	0.918	0.912
c (nm)	0.679	0.680	0.683	0.686	0.688
V (nm)^3	0.515	0.513	0.505	0.500	0.496
ρ (g cm^{-3})	3.159	3.176	3.193	3.210	3.228
Experimental					
a (nm)	0.937	0.939	0.935	0.938	0.936
c (nm)	0.682	0.686	0.681	0.684	0.684
V (nm)^3	0.518	0.523	0.515	0.521	0.518
X_C%	80.0	84.1	82.8	89.8	89.5
L_S (nm)	29.06	34.54	31.73	23.67	34.14
L_{WH} (nm)	47.81	45.91	39.28	24.94	47.81
$\varepsilon \times 10^{-3}$	0.17	−0.37	−3.19	−0.18	0.69
σ (MPa)	−142.12	120.99	108.06	−152.56	−84.13
u (kJ m^{-3})	208.8	92.4	132.2	130.4	41.2

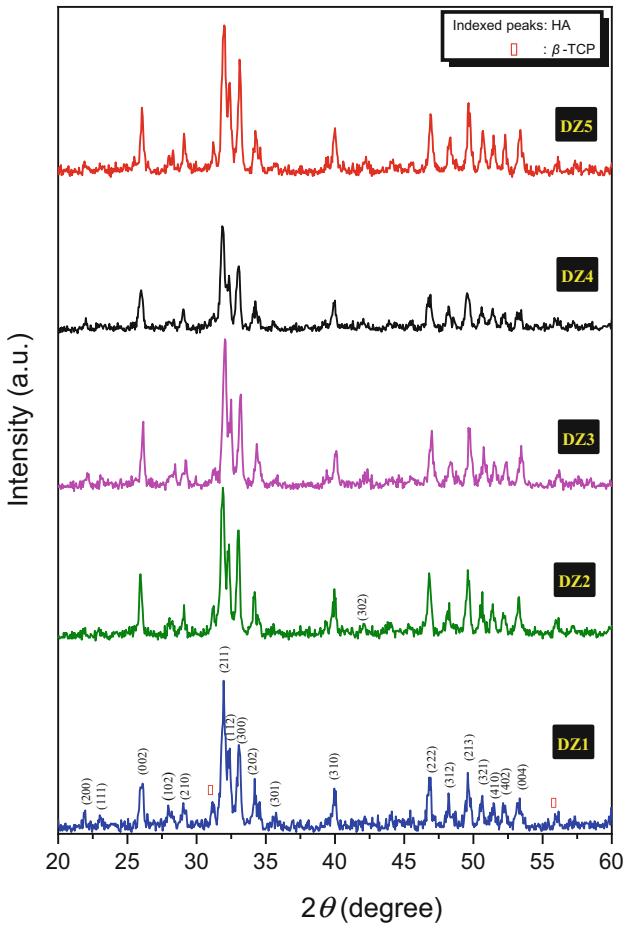

Figure 3. XRD patterns of as-produced HAps.

conduction bands, signifying the energy required to transition an electron from the valence band to the conduction band.

Previous research has explored the effect of various dopants on the properties of hydroxyapatite (HAp). Specifically, studies have investigated the utilization of dopants, such as Pr [47], Ce [48], Sm [50], Tb [51], Ti [52], Bi [53] and Yb [54]. Interestingly, it was observed that the incorporation of these dopants led to a similar decrease in their respective amounts within the HAp structure. However, when Dy was added as a dopant, a step-like decrease was observed instead. The reduction in BG energy associated with these dopants can be attributed to the alteration of electron states along symmetry lines within the material. Dopants have the ability to introduce additional electronic energy levels or modify existing ones, leading to changes in the BG value. These modifications in the electron states can result in fluctuations in the BS, ultimately influencing the BG energy. To provide further insight into the electronic properties, the DOS is depicted in the second column of each graphical representation. These figures serve to emphasize the dependence of the BG on the presence of these performance-enhancing substances. The variations in the DOS profiles offer valuable information about the distribution and availability of electron states within the material, enabling a deeper understanding of the impact of dopants on the BS and BG energy.

3.2 *LAC calculations*

LAC can be determined using the equation $I = I_0 e^{-\mu x}$, where I_0 represents the initial number of photons, I denotes the number of photons transmitted over a distance of x and μ is the LAC. The LAC of a material is a crucial parameter for applications involving radiation shielding. In such applications, materials with higher LAC values are preferred as they provide greater protection against radiation

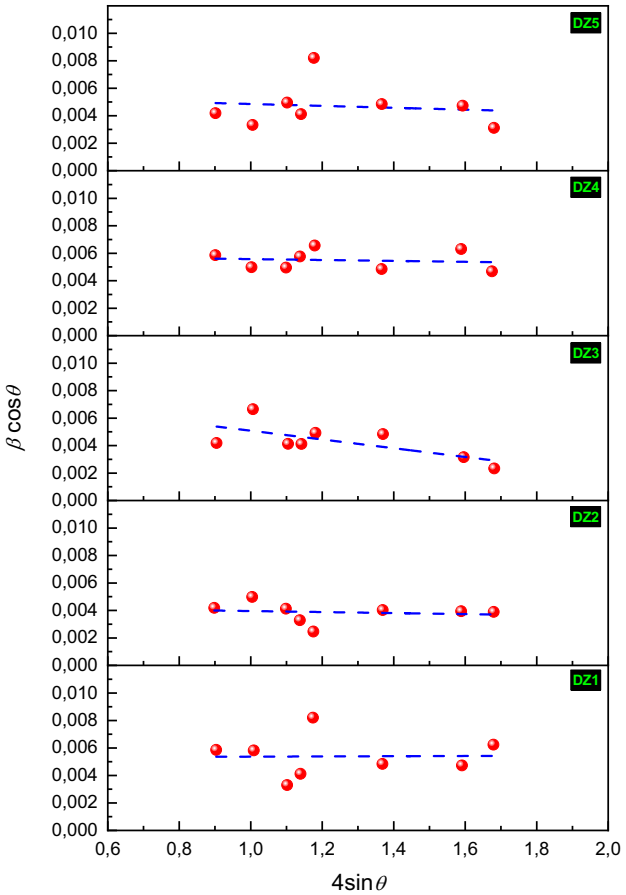

Figure 4. β cos θ *vs.* 4 sin θ plots of the samples.

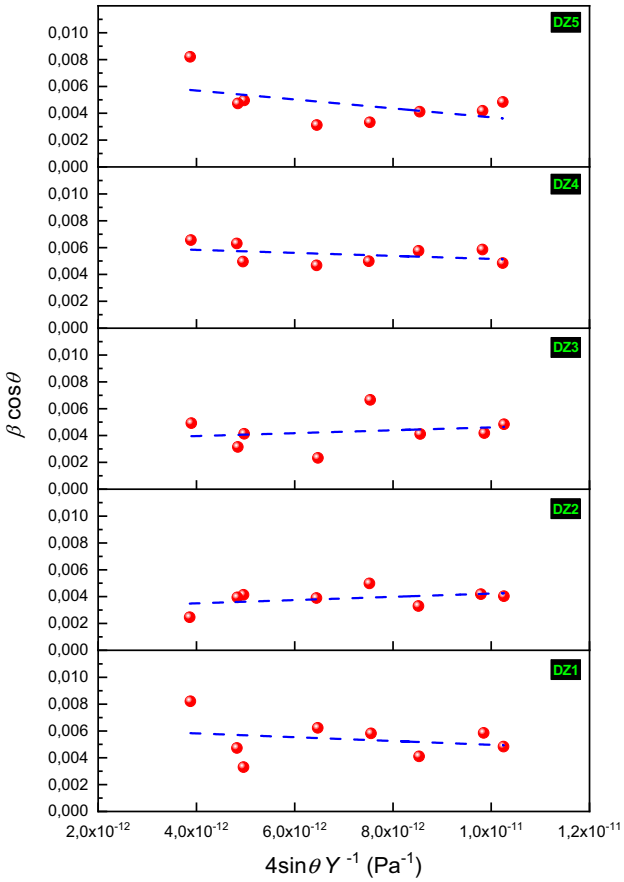

Figure 5. β cos θ *vs.* 4 sin θ Y^{-1} graphs of the samples.

[55,56]. Figure 2 displays the graphs depicting the LAC as a function of photon energy for each structure under investigation. Notably, the addition of Dy to the HAp structure leads to an increase in the radiation-shielding effectiveness of the material. This suggests that the presence of Dy enhances the material's ability to attenuate or absorb radiation. Table 1 provides the density values for each HAp structure. It is observed that the density increases as the amount of Dy incorporated into the HAp structure increases. This rise in density can be attributed to the fact that both Dy (with a density of 8.550 g cm^{-3}) and Zn (with a density of 7.134 g cm^{-3}) have higher densities compared to Ca (with a density of 1.550 g cm^{-3}) [48,57]. The increase in density due to the presence of Dy contributes to the overall radiation-shielding effectiveness of the HAp structure, as it enhances the interaction between the material and incident radiation, leading to improved attenuation properties.

3.3 *Experimental results*

3.3a *XRD analysis:* Figure 3 depicts each XRD motifs of HAps. In all the specimens, the HAp (JCPDS no: 09-0432) has its own hexagonal crystal structure and a major phase, and beta-tricalcium phosphate (β-TCP, (JCPDS no: 09-0169) has the minor one.

The lattice parameters and unit cell volume (a, c and V) can be calculated as:

$$\frac{1}{d^2} = \frac{4}{3}\left(\frac{h^2 + hk + k^2}{a^2}\right) + \frac{l^2}{c^2}, \tag{4}$$

$$V = 0.866a^2c. \tag{5}$$

Here, d is the interplanar spacing. The experimental lattice parameters and volume values have been changed with the addition of Dy (table 1). While gradual changes were calculated for the a, c and V parameters in the theoretical calculations, non-gradual changes were seen in the experimental values. This can be explained by the fact that the theoretical calculations include the as-expected results, but the experimental ones may vary with lots of parameters. Similar changes related to the formation of the secondary phase of β-TCP and its amount were reported for Dy-doped HAps [58]. The existence of an orthorhombic phase in the hexagonal crystal structure may cause the formation of lattice defects. The ionic radius of the Dy^{3+} ion is less than that of Ca^{2+} ion (100 pm), hence, the downward trend in these parameters is predicted theoretically [59,60].

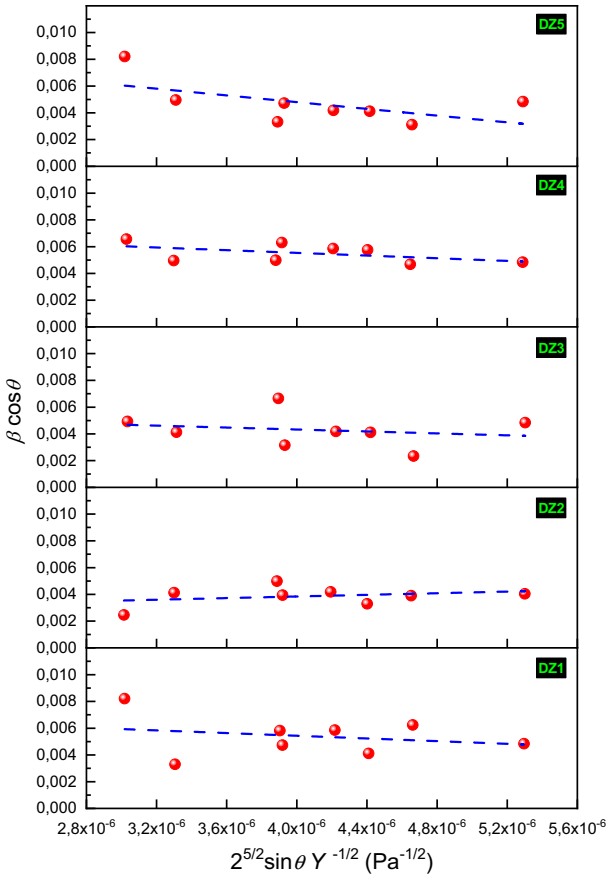

Figure 6. $\beta \cos\theta$ *vs.* $2^{5/2} \sin\theta\, Y^{-1/2}$ plots of the samples.

The crystallite size (L_S) can be estimated with the Scherrer equation [61];

$$L_S = \frac{0.9\lambda}{\beta \cos\theta}. \tag{6}$$

Here, the λ of the incident X-rays is 0.154056 nm. Williamson–Hall (WH) equation has been used to calculate the crystallite size (L_{WH}) and strain (ε) analyses [62]. With the inclusion of Dy, the values for both L_S and L_{WH} exhibit a similar trend:

$$\beta \cos\theta = \frac{0.9\lambda}{L_{WH}} + 4\varepsilon \sin\theta. \tag{7}$$

σ, lattice stress and Y, Young's modulus were calculated with

$$\beta \cos\theta = \frac{0.9\lambda}{L_{WH}} + \frac{4\sigma \sin\theta}{Y}, \tag{8}$$

$$\beta \cos\theta = \frac{0.9\lambda}{L_{WH}} + 4 \sin\theta \left(\frac{2u}{Y}\right)^{1/2}. \tag{9}$$

The parameters used here are: β is the full width at half-maximum wavelength (λ), θ the Bragg angle and u the anisotropic energy density. The values of $\beta \cos\theta$ *vs.* $4 \sin\theta$, $\beta \cos\theta$ *vs.* $4 \sin\theta\, Y^{-1}$ and $\beta \cos\theta$ *vs.* $2^{5/2} \sin\theta\, Y^{-1/2}$ shown in figures 4, 5 and 6, have been used to calculate the L_{WH}, ε, σ and u values. Four characteristics are considerably impacted by Dy-content, as shown in table 1, indicating that the crystal structure is under compressive stress [63]. The crystallinity percent (X_C%) [64]:

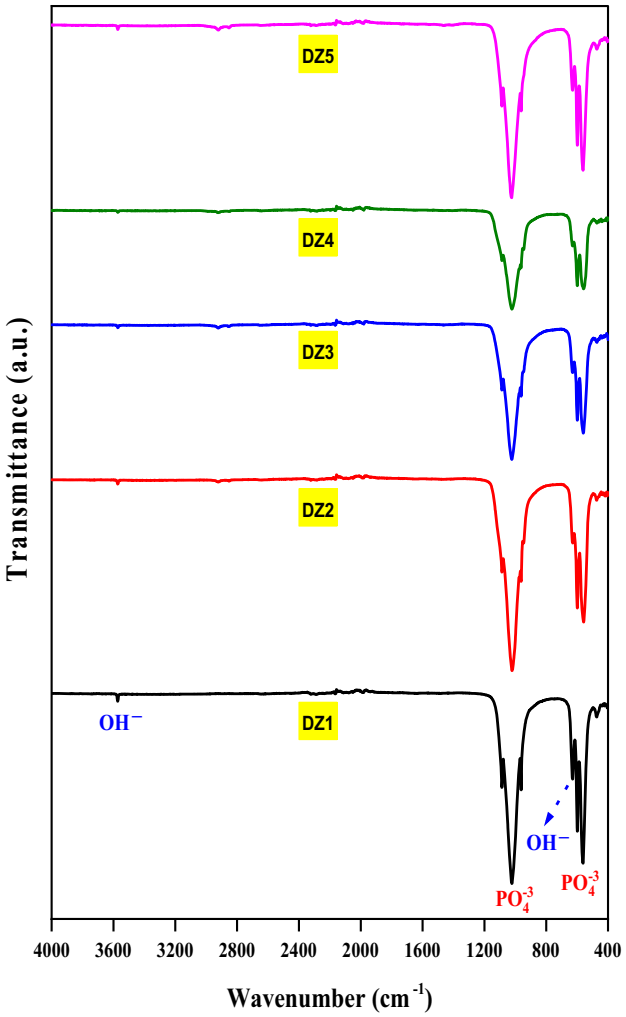

Figure 7. FTIR spectra of the as-prepared HAps.

$$X_C\% = \left(1 - \frac{V_{112/300}}{I_{300}}\right) \times 100, \tag{10}$$

Here, $V_{112/300}$ is the intensity of the hollow between (112) and (300) peaks and I_{300} is the intensity of (300) peak. All the X_C% values were calculated in the range of 80.0 and 89.8 and affected by the amount of Dy-dopant. With an increase in Dy, this parameter changes non-gradually.

3.3b *FTIR and Raman results:* Figures 7 and 8 depict the FTIR and Raman analyses results for pure and doped samples. Since the phosphate and hydroxyl groups of the HAp were found in the typical bands, these results demonstrate that the HAp structure is present in each

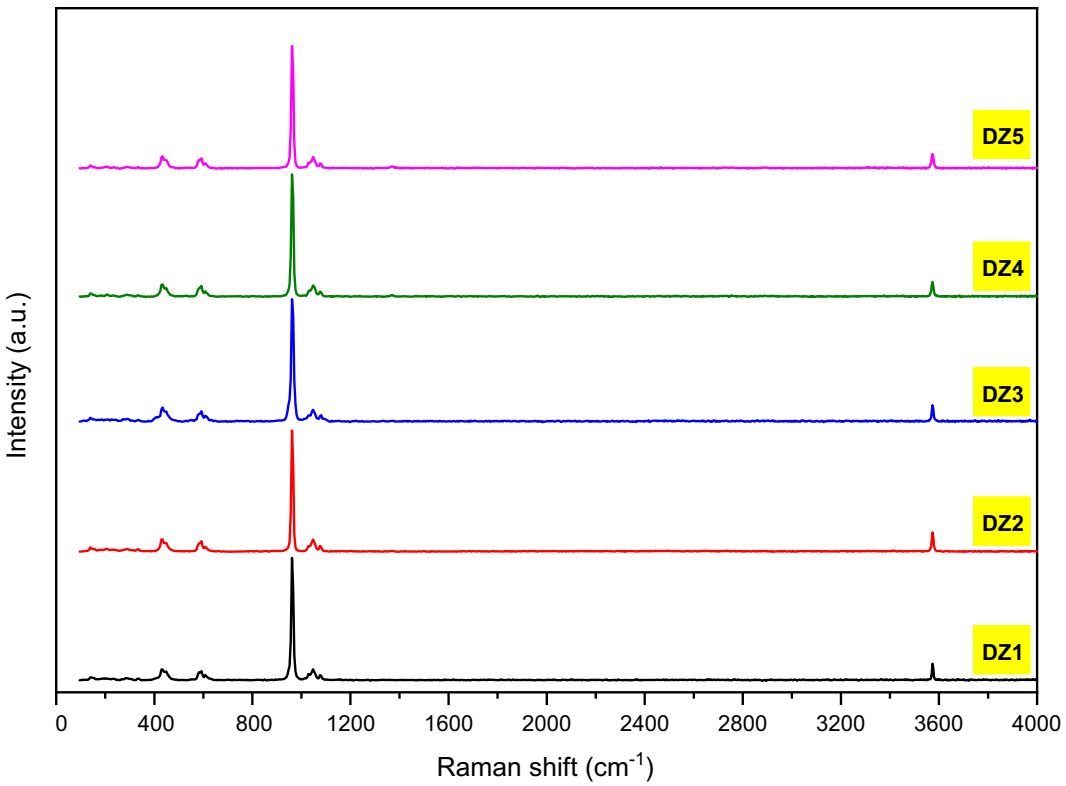

Figure 8. Raman spectra of the as-synthesized HAp samples.

sample. Both spectra showed the presence of bands associated to the PO_4^{3-} group around 1100–400 cm^{-1}, which are caused by symmetric and asymmetric stretchings and bending vibration modes, respectively [65–71]. In the FTIR, the bands of 1086, 1022, 962, 599 and 562 cm^{-1} were detected, while the bands of 1076, 1047, 962, 607, 592 and 433 cm^{-1} in Raman. In FTIR spectra, the bands associated with the OH^- group were seen around 630 and 3573 cm^{-1} and in Raman spectra, the band was observed only at 3574 cm^{-1} [48,50].

3.3c *SEM results:* The investigation of nanoparticle morphology plays a crucial role in understanding their physical and chemical properties as well as their potential applications. In this study, we utilized scanning electron microscopy (SEM) and energy-dispersive X-ray spectroscopy (EDX) analyses to examine the as-produced samples. The SEM images provided high-resolution visualizations of the samples, enabling the characterization of their surface features and structural characteristics. Notably, the samples exhibited spherical nanoparticle morphologies, appearing in both isolated and aggregated forms. The SEM analysis revealed diverse nanoparticle sizes and uniform distribution throughout the samples. Moreover, EDX analysis was employed to determine the elemental composition of the nanoparticles. The results from the EDX analysis provided valuable insights into the chemical constituents present in the samples, allowing for a deeper understanding of their composition. The combination of SEM images and EDX analysis findings, as illustrated in figure 9, offers a comprehensive overview of the morphology and elemental composition of the as-produced samples. These results serve as a foundation for further investigations and discussions regarding the properties and potential applications of these spherical nanoparticles. Miculescu *et al* [72] and Lett *et al* [73] indicate the sources from which the methodology and techniques used in this study were derived.

3.3d *Thermal analysis:* Thermal stability of the samples was assessed by subjecting them to a differential thermal analysis (DTA) from room temperature to 900°C, as illustrated in figure 10. The DTA curves obtained during this temperature range revealed an absence of any discernible peaks associated with significant changes, such as melting or phase transitions in the samples. This indicates that the samples exhibit thermally stable behaviour within the examined temperature range. The absence of any distinct thermal events suggests that the samples possess a high degree of structural integrity and resistance to thermal degradation. These findings are valuable in understanding the thermal properties and potential applications of the samples, as their ability to withstand high temperatures without undergoing substantial transformations is of significant interest in various fields, including materials science and engineering.

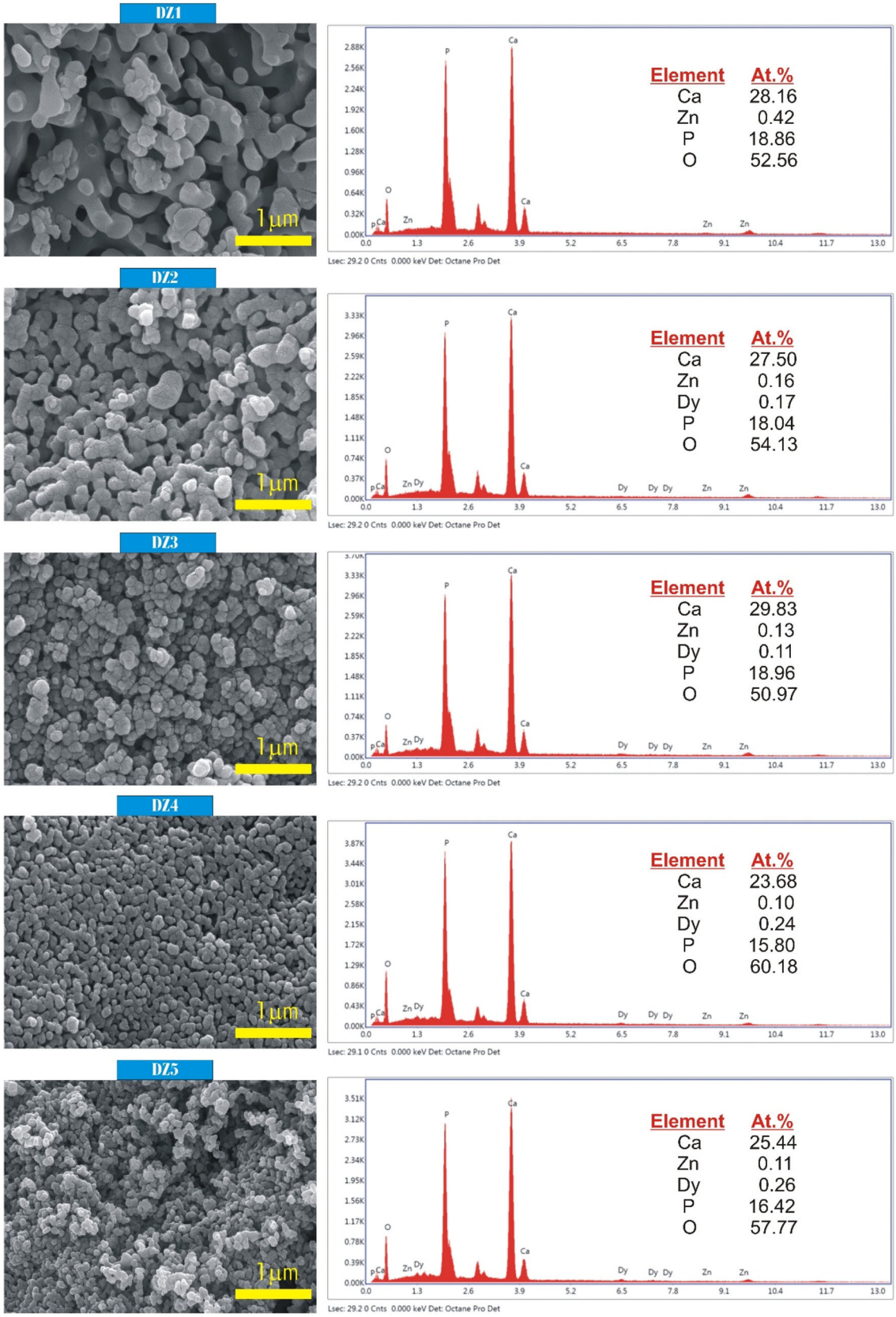

Figure 9. SEM photos and EDX results of the samples.

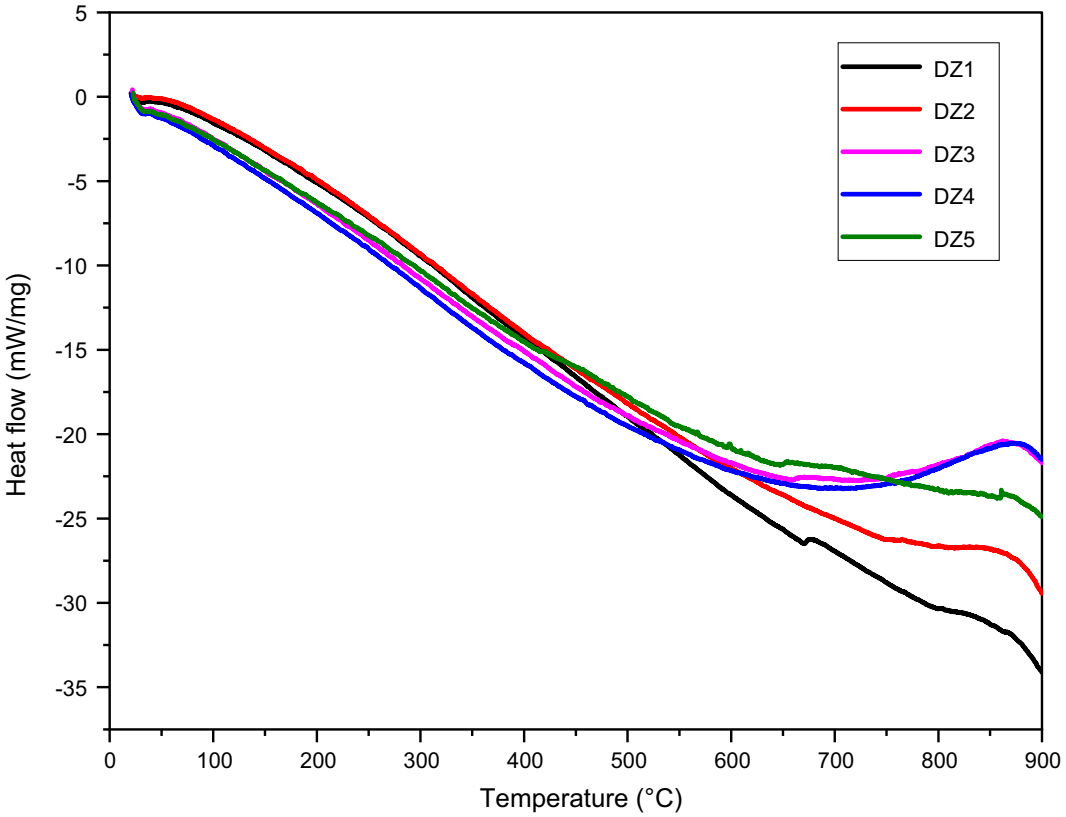

Figure 10. DTA curves of the as-prepared samples.

3.3e *Biocompatibility results:* Cell viability results given in figure 11 showed that the biocompatibility of the materials is over 80%. According to the ISO-10993-5 standard, more than 30% reduction in cell viability is evaluated as a cytotoxic effect for a biomaterial. Hereby, it can say that the biocompatibilities of the as-prepared samples fall in the acceptable range. A continuous decrease from 99.42 to 82.31% in the cell viability was seen. Similar trend was detected for the Dy-doped HAps having Dy at increasing amount from 0.22 to 0.88 at.% with a step of 0.22 at.% [58]. In the present study, we used higher amounts of Dy compared to the as-reported study and observed its lower negative effect. The use of Zn with Dy contributes in improving the cell viability of Dy-containing HAps. This gradual decrease in the cell viability is possible due to the release of Dy ions from the samples. It can be concluded that excessive amounts of a single dopant of Dy can be dangerous to health.

4. Conclusions

This study investigated the effects of Dy-content on the structural, spectroscopic and *in vitro* cell survival aspects of Zn-based hydroxyapatite (HAp) specimens synthesized through the wet chemical approach. Theoretical analysis was conducted to study the bond strength and DOS of each sample, while experimental results were used to determine the impacts of Dy-content on various properties. The variables a, c and V exhibited non-gradual changes in their actual values, but the theoretically derived values for a and V demonstrated a consistent downward trend. Additionally, the BG values showed a continuous decrease, indicating the growth of localized atomic charges. Moreover, the Dy-doped samples exhibited smaller crystallite diameters compared to the undoped samples. The stoichiometry and thermal stability of the specimens remained relatively unchanged, and the biocompatibility of each sample was evaluated. Interestingly, an increase in the amount of Dy resulted in a decrease in cell viability, suggesting a negative impact on the survival of cells *in vitro*. These findings provide valuable insights into the structural, spectroscopic and biological properties of Dy-doped Zn-based HAp, paving the way for potential applications in the fields of biomedical and materials science. Further studies can build upon these results to explore the mechanisms behind the observed effects and to optimize the synthesis of Dy-doped HAp materials for specific applications.

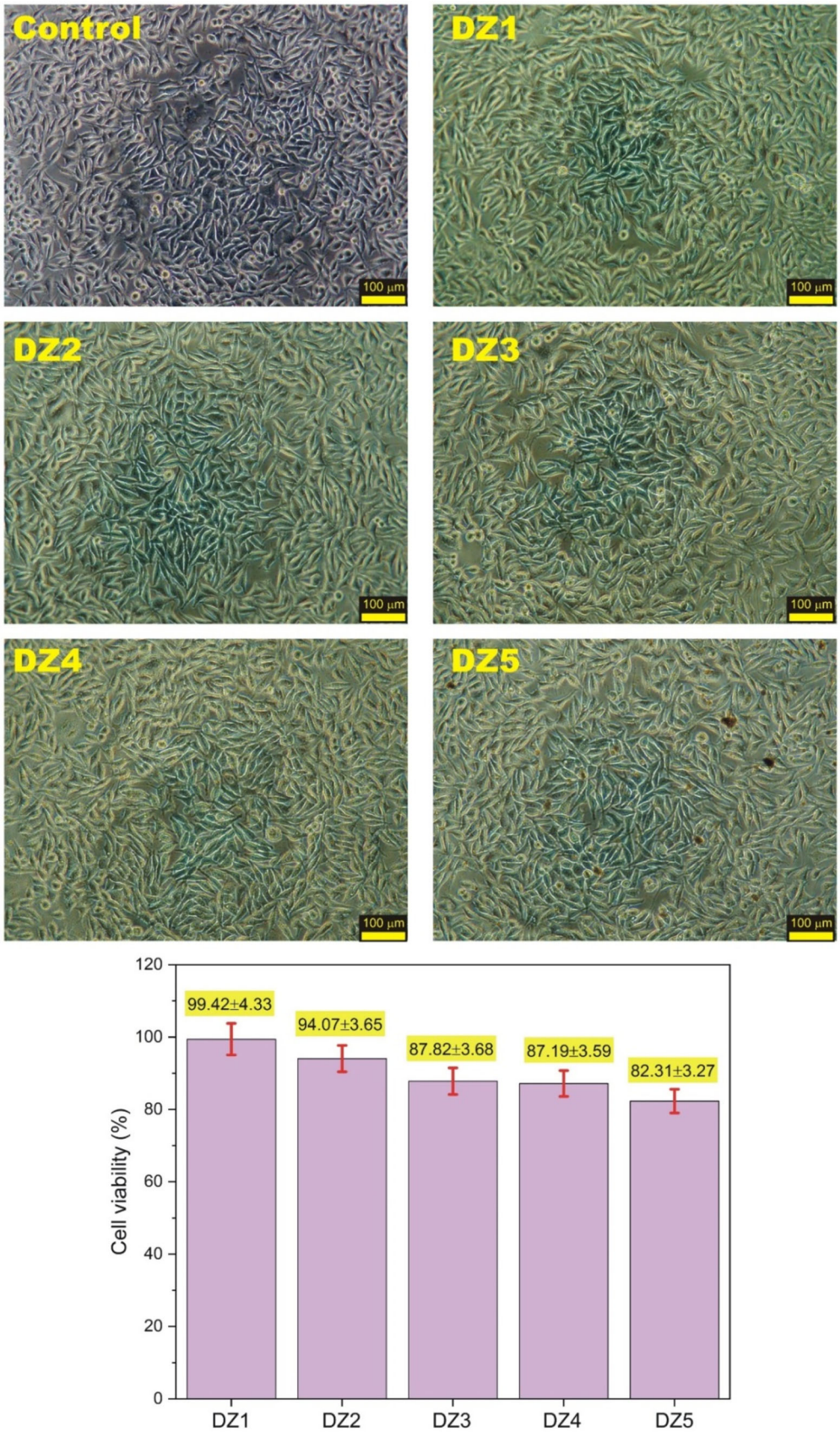

Figure 11. TGA curves of the as-synthesized samples.

Acknowledgements

This work was supported by the Management Unit of Scientific Research Projects of Firat University (FUBAP) (Project Nos.: FF.21.33, FF.23.13 and FF.23.12).

References

[1] Hossain M S, Uddin M N, Sarkar S and Ahmed S 2022 *J. Saudi Chem. Soc.* **26** 101559
[2] Sahraoui T, Chouia F, Bourezg Y I and Guelil A 2022 *Mater. Chem. Phys.* **292** 126865
[3] Hussin M S F, Abdulah H Z, Idris M I and Wahap M A A 2022 *Heliyon* **8** e10356
[4] Laonapakul T, Suthi T, Otsuka Y, Mutoh Y, Chaikool P and Chindaprasirt P 2022 *Arab. J. Chem.* **15** 104220
[5] Mobarak M B, Hossain M S, Yeasmin Z, Mahmud M, Rahman M M, Sultana *et al* 2022 *J. Mol. Struct.* **1252** 132142
[6] Uematsu M, Ishii K, Sameshima H, Ito M, Nguyen T K N, Ishigaki T *et al* 2022 *Mater. Lett.* **326** 132939
[7] Rout A and Agrawal S 2022 *Optik* **249** 168217
[8] Astala R and Stott M J 2005 *Chem. Mater.* **17** 4125
[9] Wang X and Han Y 2023 *Comput. Mater. Sci.* **224** 112153
[10] Hartati Y W, Irkham I, Zulqaidah S, Syafira R S, Kurnia I, Noviyanti A R *et al* 2022 *Sens. Bio-Sens. Res.* **38** 100542
[11] Wang B, Yan X, Xu Y, Zhou H and Shi G 2022 *Mater. Today Commun.* **33** 104773
[12] Jiang Z, Gong Z, Song W, Wu P, Deng C, Chen Q *et al* 2022 *Inorg. Chem. Commun.* **146** 109860
[13] Lakrat M, Jodati H, Mejdoubi E M and Evis Z 2023 *Powder Technol.* **413** 118026
[14] Chatterjee T, Chatterjee P, Chakraborty A K, Pradhan S K and Meikap A K 2022 *Mater. Today Commun.* **33** 104870
[15] Nisar A, Iqbal S, Rehman M A U, Mahmood A, Younas M, Hussain S Z, Tayyaba Q *et al* 2023 *Mater. Chem. Phys.* **299** 127511
[16] Herradi S, Adouar I, Bouhazma S, Chajri S, Khaldi M, El Bali B *et al* 2022 *Mater. Today Proc.* **53** 413
[17] Gomez-Vazquez O M, Correa-Piña B A, Zubieta-Otero L F, Castillo-Paz A M, Londoño-Restrepo S M and Rodriguez-García M E 2021 *Ceram. Int.* **47** 32775
[18] Zhu D, Wang J and Hu W 2022 *Colloids Surf. A: Physicochem. Eng. Asp.* **647** 129075
[19] Xiao Q, Zhou K, Chen C, Jiang M, Zhang Y, Luo H *et al* 2016 *Mater. Sci. Eng. C* **69** 1068
[20] Orooji Y, Mortazavi-Derazkola S, Ghoreishi S M, Amiri M and Salavati-Niasari M 2020 *J. Hazard. Mater.* **400** 123140
[21] Shih W J, Chen Y F, Wang M C and Hon M H 2004 *J. Cryst. Growth* **270** 211
[22] Chen B H, Chen K I, Ho M L, Chen H N, Chen W C and Wang C K 2009 *Mater. Chem. Phys.* **113** 365
[23] Liang T, Qian J, Yuan Y and Liu C 2013 *J. Mater. Sci.* **48** 5334
[24] Ferrairo B M, Mosquim V, de Azevedo-Silva L J, Pires L A, Padovini D S S, Magdalena A G *et al* 2023 *Mater. Chem. Phys.* **295** 127046
[25] Ezerskyte-Miseviciene A and Kareiva A 2019 *Mendeleev Commun.* **29** 273
[26] Adamu D B, Zereffa E A, Segne T A, Razali M H and Lemu B R 2023 *Environ. Adv.* **12** 100360
[27] Xu Y, Tang H, Wu P, Chen M, Shang Z, Wu J *et al* 2023 *Chemosphere* **321** 138123
[28] Jodati H, Evis Z, Tezcaner A, Alshemary A Z and Motameni A 2023 *J. Mech. Behav. Biomed. Mater.* **140** 105722
[29] Ateş H G, Kaygili O, Bulut N, Osmanlıoğlu F, Keser S, Tatar B *et al* 2023 *J. Mol. Struct.* **1283** 135318
[30] Chen L, Wang Y, Cao X, Zhang Z and Liu Y 2023 *J. Solid State Chem.* **317** 123687
[31] Han J, Qi J, Du J and Zhang G 2020 *Mater. Lett.* **278** 128415
[32] Zhou H, Xie Y, Wang X, Yang H, Wang Y and Zhang Y 2022 *Environ. Technol. Innov.* **25** 102103
[33] Ercan I, Kaygili O, Kayed T, Bulut N, Tombuloğlu H, İnce T *et al* 2022 *Phys. B: Condens. Matter* **625** 413486
[34] Daood U and Fawzy A 2023 *J. Mech. Behav. Biomed. Mater.* **140** 105737
[35] Nenen A, Maureira M, Neira M, Orellana S L, Covarrubias C and Moreno-Villoslada I 2022 *Ceram. Int.* **48** 34750
[36] Karunakaran G, Cho E B, Kumar G S, Kolesnikov E, Govindaraj S K, Mariyappan K *et al* 2023 *Environ. Res.* **216** 114683
[37] Bulcar K, Oglakci M, Yücel A, Sezer S, Madkhali O, Depci T *et al* 2023 *J. Lumin.* **255** 119619
[38] Mondal S, Nguyen V T, Park S, Choi J, Tran L H, Yi C Y *et al* 2020 *Ceram. Int.* **46** 16020
[39] Herradi S, Adouar I, Bouhazma S, Chajri S, Khaldi M, El Bali B *et al* 2022 *Mater. Today Proc.* **53** 386
[40] Nardi M V, Timpel M, Biondani E, Ceccato R, Chiappini A and Dirè S 2021 *Op. Mater. X* **12** 100118
[41] Ofudje E A, Adeogun A I, Idowu M A and Kareem S O 2019 *Heliyon* **5** e01716
[42] Buyuksungur S, Huri P Y, Schmidt J, Pana I, Dinu M, Vitelaru C *et al* 2023 *Ceram. Int.* **49** 12570
[43] Uysal I, Yilmaz B and Evis Z 2021 *J. Aust. Ceram. Soc.* **57** 869
[44] Tesch A, Wenisch C, Herrmann K H, Reichenbach J R, Warncke P, Fischer D *et al* 2017 *Mater. Sci. Eng. C* **81** 422
[45] Lafarga A K S, Moisés F P P, Gurinov A, Ortiz G G and Arízaga G G C 2015 *Mater. Sci. Eng. C* **48** 541
[46] Kaygili O, Vural G, Keser S, Yahia I S, Bulut N, Ates T *et al* 2021 *J. Aust. Ceram. Soc.* **57** 305
[47] Agid R S, Kaygili O, Bulut N, Dorozhkin S V, Ates T, Koytepe S *et al* 2020 *J. Aust. Ceram. Soc.* **56** 1501
[48] Kareem R O, Kaygili O, Ates T, Bulut N, Koytepe S, Kuruçay A *et al* 2022 *Ceram. Int.* **48** 33440
[49] Clark S J, Segall M D, Pickard C J, Hasnip P J, Probert M I J, Refson K *et al* 2005 *Z. Kristallogr. Cryst. Mater.* **220** 567
[50] Hssain A H, Bulut N, Ates T, Koytepe S, Kuruçay A, Kebiroglu H *et al* 2022 *J. Aust. Ceram. Soc.* **58** 1491
[51] Jiménez-Flores Y, Suárez-Quezada M, Rojas-Trigos J B, Lartundo-Rojas L, Suárez V and Mantilla A 2017 *J. Mater. Sci.* **52** 9990
[52] Tsukada M, Wakamura M, Yoshida N and Watanabe T 2011 *J. Mol. Catal. A: Chem.* **338** 18
[53] Korkmaz A A, Ahmed L O, Kareem R O, Kebiroglu H, Ates T, Bulut N *et al* 2022 *J. Aust. Ceram. Soc.* **58** 803
[54] Acar S, Kaygili O, Ates T, Dorozhkin S V, Bulut N, Ates B *et al* 2022 *Mater. Chem. Phys.* **276** 125444
[55] Shkir M, AlFaify S, Yahia I S, Ganesh V and Shoukry H 2017 *Phys. B: Condens. Matter* **508** 41

[56] Alsmadi Z Y and Bourham M 2020 *Int. J. Phys. Res.* **10** 11
[57] Gómez-Ros J M, Bedogni R, Palermo I, Esposito A, Delgado A, Angelone M *et al* 2011 *Radiat. Meas.* **46** 1712
[58] Isen F, Kaygili O, Bulut N, Ates T, Osmanlıoğlu F, Keser S *et al* 2023 *J. Aust. Ceram. Soc.* **59** 849
[59] Cawthray J F, Creagh A L, Haynes C A and Orvig C 2015 *Inorg. Chem.* **54** 1440
[60] Yu J, Wang Y, Dai Z, Yang F, Fallahpour A and Nasiri-Tabrizi B 2021 *Ceram. Int.* **47** 9034
[61] Scheverin V N, Horst M F and Lassalle V L 2022 *Results Eng.* **16** 100648
[62] Venkateswarlu K, Bose A C and Rameshbabu N 2010 *Phys. B* **405** 4256
[63] Zak A K, Majid W A, Abrishami M E and Yousefi R 2011 *Solid State Sci.* **13** 251
[64] Landi E, Tampieri A, Celotti G and Sprio S 2000 *J. Eur. Ceram. Soc.* **20** 2377
[65] El-Naggar M E, Abu Ali O A, Saleh D I, Abu-Saied M A, Ahmed M K, Abdel-Fattah *et al* 2022 *J. Lumin.* **37** 290
[66] Huang S, Chen C, Zhao Z, Jia L and Zhang Y 2023 *Chemosphere* **312** 137226
[67] Kaygili O 2019 *J. Aust. Ceram. Soc.* **55** 381
[68] Jiang X, Liu X, Cai J, Wei S, Wang Y, Duan Z *et al* 2023 *Colloids Surf. B* **222** 113097
[69] Erdem U, Dogan D, Bozer B M, Turkoz M B, Yıldırım G and Metin A U 2022 *J. Mech. Behav. Biomed. Mater.* **136** 105517
[70] Pecheva E V, Pramatarova L D, Maitz M F, Pham M T and Kondyuirin A V 2004 *Appl. Surf. Sci.* **235** 176
[71] Ciobanu C S, Predoi D, Chapon P, Predoi M V and Iconaru S L 2021 *Coatings* **11** 1466
[72] Miculescu F, Luţă C, Constantinescu A E, Maidaniuc A, Mocanu A C, Miculescu M *et al* 2020 *J. Funct. Biomater.* **11** 82
[73] Lett J A, Sundareswari M, Ravichandran K, Latha M B, Sagadevan S and Johan M R B 2019 *RSC Adv.* **9** 6228